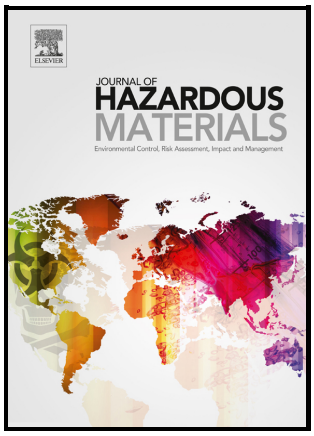

Release and mobility of hexavalent chromium in contaminated soil with chemical factory waste: experiments, Cr isotope analysis and reactive transport modeling

Elina Ceballos, Jordi Cama, Josep M. Soler, Robert Frei

PII: S0304-3894(23)00475-2

DOI: https://doi.org/10.1016/j.jhazmat.2023.131193

Reference: HAZMAT131193

To appear in: *Journal of Hazardous Materials*

Received date: 24 January 2023
Revised date: 5 March 2023
Accepted date: 9 March 2023

Please cite this article as: Elina Ceballos, Jordi Cama, Josep M. Soler and Robert Frei, Release and mobility of hexavalent chromium in contaminated soil with chemical factory waste: experiments, Cr isotope analysis and reactive transport modeling, *Journal of Hazardous Materials,* (2023) doi:https://doi.org/10.1016/j.jhazmat.2023.131193

Release and mobility of hexavalent chromium in contaminated soil with chemical factory waste: experiments, Cr isotope analysis and reactive transport modeling

Elina Ceballos[1,*], Jordi Cama[2], Josep M. Soler[2], Robert Frei[3]

[1] *Instituto de Hidrología de Llanuras "Dr. Eduardo J. Usunoff"(IHLLA), CONICET-UNCPBA-CIC, 7300 Azul, Buenos Aires, Argentina*

[2] *Institute of Environmental Assessment and Water Research (IDAEA), CSIC, 08034 Barcelona, Catalonia, Spain*

[3]*Department of Geosciences and Natural Resource Management, University of Copenhagen, Copenhagen, Denmark*

Submitted to:

Journal of Hazardous Materials

*Corresponding author (eceballos@ihlla.org.ar)

ABSTRACT

Our study focused on the leaching processes in soil contaminated with hexavalent chromium (Cr(VI)), traced to industrial waste from a disused site and resulting in groundwater contamination. Mineral and geochemical characterization of the soil by means of XRD, SEM-EDS, total digestion and sequential extractions revealed that the main Cr content was from solid waste located in the upper meter of the soil profile. Flow-through and column experiments were carried out to investigate the processes responsible for Cr(VI) release. Cr(VI) mobility along the soil profile was also assessed. Moreover, Cr isotope signatures were used to evaluate a potential Cr(VI) reduction process, which preferably could immobilize toxic Cr(VI) complexes. One-dimensional (1D) numerical simulations reproduced the Cr(VI) release from the flow-through experiment containing the Cr(VI) rich-solid waste and also the Cr(VI) mobility along the column experiment. These results enabled us to interpret quantitatively the processes resulting in Cr(VI) contamination and mobility along the soil profile. Cr(VI) was released from dissolving Cr(VI)-rich phases (e.g., sodium chromate, Cr(VI)-hydrocalumite and Cr(VI)-ettringite) of the solid waste layer. Cr(VI) reduction and Cr(VI) adsorption did not take place along the column. Such accurate characterization of these processes is necessary for the mitigation of Cr(VI) mobility in contaminated soils.

Keywords: hexavalent chromium, contamination, soil, reactive transport modeling

1. INTRODUCTION

Chromium (Cr) is a contaminant in groundwater and soil mostly derived from anthropogenic activities such as electroplating, pigment and chemical industries, which are a source of Cr(VI), and tannery industries, which are a source of Cr(III). These industries generate large amounts of Cr wastes in effluents, sludge and solid residue. Cr(VI) is more toxic and generally more mobile than Cr(III) and may cause cancer and dermatitis (Kotas and Stasicka, 2000). However, Cr(III) is an essential nutrient, is less soluble and adsorbs strongly on solid surfaces (Rai et al., 1989).

Chromium-ore processing residue (COPR) is a solid waste generated by basic chromium sulfate (BCS)-producing industries. The waste is alkaline (Geelhoed et al., 2002) and ~ 30% of the total Cr is present as Cr(VI) (Farmer et al., 2006). COPR is a complex mixture of crystalline phases together with an amorphous component and Cr(VI) present in several forms. According to Hillier et al. (2003), minerals and compounds identified in COPR fall into three groups: the first group includes only one mineral, chromite, which can only be a relict of primary chromium ore; the second one consists of minerals that form at high temperatures attained during the extraction process; and the third group includes solid phases formed during the exposure of COPR to ambient operating conditions and to leaching.

Geelhoed et al. (2002) identified the solid phases in COPR exposed to different pH conditions (e.g. pH between 8 and 12) during batch experiments. Cr(VI)-hydrocalumite, Cr(VI)-bearing hydrogarnet, magnesiochromite, periclase, brownmillerite, calcite, and brucite were found between pH 10 and 12. Cr(VI)-ettringite, $CaAl_2(OH)_8 \cdot 6H_2O$, wairakite, dolomite and amorphous $Al(OH)_3$ were identified between pH 8 and 10. Furthermore, these authors observed that by lowering the pH, the dissolution of Cr(VI)-hydrocalumite and Cr(VI)-bearing hydrogarnet results in the release of Cr(VI). The mineralogical characteristics and solid-phase speciation of Cr in COPR deposits have been widely studied (Bhattacharya et al., 2019; Marten et al., 2016; Foldi et al., 2013; Boecher et al., 2012; Chrysochoou et al., 2009; Chrysochoou and Dermatas, 2007; Geelhoed et al., 2002; Hillier et al., 2003; Thomas et al., 2001) but the mechanisms and the kinetics of Cr release from COPR remain to be clarified.

COPR materials are usually treated to immobilize Cr(VI) before disposal (Du and Chrysochoou, 2020; Mo et al., 2020; Zhang et al., 2018). The most widely used

techniques are based on the reduction of Cr(VI) to Cr(III) by using reductants such as ferrous sulfate and polysulfide. However, a number of studies have shown that reduced COPR (rCOPR) cannot attain long-term stability, giving rise to slow and continuous release of residual Cr(VI) during subsequent deposition (51.6 mg L^{-1}; Liu et al., 2020). Song et al. (2019) indicated that ettringite is the typical Cr(VI) host phase in rCOPR treated with ferrous sulfate, which suggests that this phase is not sufficiently stable under different concentrations of carbonate, sulfate, acid solutions and temperature.

COPR and rCOPR materials are not stable during precipitation events given the release of Cr(VI) by dissolution of the mineral phases and consequent leaching to groundwater. Earlier studies carried out in New Jersey (USA) (Burker et al., 1991), Glasgow (UK) (Farmer et al., 1999) and Kanpur (India) (Singh et al., 2009) provide ample evidence of Cr(VI) contamination in groundwater, suggesting that the source of contamination is COPR. Ceballos et al. (2018) detected Cr(VI) contamination in groundwater in an industrial area of the Matanza-Riachuelo basin (MRB), Argentina. In this study, these authors indicated that the main source of Cr(VI) contamination was traced to a chemical plant that produced bichromates, chromic acid and tanning products. Subsequently, Ceballos et al. (2020) evaluated the processes that control the natural attenuation of Cr(VI) in the groundwater by determining the isotopic fractioning in the laboratory and measuring the isotopic field data. During the plant-operation period, the untreated residues were discharged into nearby unlined piles, where dissolution of these waste salts promoted the migration of Cr(VI) through the vadose zone into groundwater. Since the closure of the plant, rain water leached the piles, resulting in a continuous alteration of the geochemistry and mineralogy of the vadose sediments. Ceballos et al. (2021) measured the total Cr and pH in the soil affected by residues from the chemical plant, where the highest concentration of total Cr was found in the soil samples with acidic pH. Dissolution of primary phases and precipitation of secondary phases incorporating Cr in their structure or adsorbing Cr on their surfaces are probable reactions. The lack of characterization of these contaminated sediments probably accounts for our scant knowledge of the geochemical processes responsible for the source of MRB groundwater contamination by Cr(VI).

The present work seeks to assess the processes that lead to Cr(VI) release in the vadose zone. A quantitative geochemical understanding is essential to characterize

the source of Cr contamination of the MRB groundwater, which is necessary for the successful application of remediation techniques. To this end, four tasks were undertaken: a) an accurate chemical and mineral characterization of the soil was performed by means of multi-acid digestion, sequential extraction and X-ray diffraction analyses to determine the phases that contain Cr; b) a series of flow-through experiments was conducted to evaluate the processes responsible for Cr(VI) release; c) a column experiment using representative soil samples obtained from the site allowed the study of Cr(VI) mobility along the soil profile and d) a characterization of chromium of the output solutions focused on the evaluation of potential Cr(VI) reduction processes. The outflow concentrations in both the flow-through and column experiments were monitored and reproduced using 1-D reactive transport modeling, which allowed us to identify and quantify the relevant processes.

2. MATERIALS AND METHODS

2.1 Soil characterization

The soil samples of this study were collected from a 30-year-old waste disposal site of a chemical factory that was active between 1968 and 1990 (Fig. S2). Drilling to collect soil samples reached 200 cm in depth. Sixteen samples were collected in total. Fifteen samples consisted of soil portions extracted every 10-20 cm along the 200-cm profile (i.e. samples #20 - #200; Table 1). From 40 cm (sample #50) to 85 cm (sample #85) green blocks (rubble) of variable dimensions were found. One block collected between 40 cm and 50 cm (sample #R6) was identified as solid waste (Table 1). All samples were dried separately at room temperature for one week in a clean environment. Thereafter, each sample was divided into four portions. The first portion was disaggregated and sieved to < 2-mm fraction for mineralogical and chemical characterization. The second one (also < 2-mm fraction) was used for sequential extraction procedure (SEP). The third portion was ground to a size fraction between 60 μm and 100 μm for use in the flow-through experiments, and the fourth portion was ground to a size fraction between 1 mm and 4 mm for use in the column experiment.

The chemical composition of the soil-waste samples collected at different depths was obtained through multi-acid digestion. About 2 g of pulverized material of each sample were completely digested with a mixture of HNO_3, $HClO_4$ and HF. The ele-

mental concentration of the solutions was measured by optical (-OES) and mass (-MS) inductively coupled plasma (ICP). The mineralogical characterization of the powdered samples selected (size fraction ≈ 50 μm) was obtained by powder X-ray diffraction (XRD)-Rietveld analysis using a Bruker D8 A25 Advance X-ray diffractometer, scanning from 0 to 60 degrees (2θ) with a constant scan speed of 0.025º/18 s and CuKα1 radiation (Table 2). The minimum amount for phase detection in XRD analysis is ≈ 3 wt%. The mineral morphology and qualitative element composition of the samples were studied by SEM-EDS. The analysis was carried out with a field emission JEOL JSM-840 instrument under a 15–20 kV, using the backscattered electron detector (BSE) and an energy-dispersive spectrometer (EDS).

2.2 Sequential extraction procedure

A sequential extraction process (SEP) was applied to characterize the total chromium (Cr) content in different mineral fractions of nine soil samples (#20, #40, #50, #60, #75, #85, #100, #110 and #200; Table 3) according to the Cr content obtained by multi-acid digestion. The SEP used was a modified version of Torres and Auleda (2013), which in turn, was based on the methods described by Dold (2003), Sposito et al. (1989), and Pagnanelli et al. (2004). Three extraction replicates were carried out using 0.5 g of dry material for each sample. The sequence of the steps, the type and amount of reagent, reaction time and temperature are summarized in Table S1 in Supporting Information (SI). After each extraction, the solution was separated from the solid by centrifugation at 3000 rpm for 15 min. Subsequently, the supernatant solutions were analyzed for Cr concentrations.

2.3 Experimental setup

In this study, six flow-through experiments and one column experiment were performed to evaluate the release of the major elements (e.g. Si, S, Ca and Cr(VI)) from the phases that make up the soil profile. Samples #20, #40, #50 and #75 corresponded to those with high Cr contents. Sample #200 represented soil without Cr and sample #R6 was solid waste. The variation in the chemical composition of the effluents as a function of time in the #R6 flow-through experiment and in the column experiment was reproduced by reactive transport simulations to quantitatively interpret

both the Cr(VI) release and Cr(VI) mobility (see section 4). Millipore MQ water (pH = 5.9) was injected in the experiments that were run at room temperature (22 ± 2 ºC).

2.3.1 Flow-through experiments

Defined amounts of sample (0.7500 ± 0.0015 g) were placed in non-stirred 32.5 mL reactors. Teflon © filters (0.22 μm) were set at the inlet and outlet of each reactor to prevent particle loss. The flow rate was held constant at ≈ 0.05 mL min^{-1} using a Gilson ® peristaltic pump, yielding a residence time within the cell of ≈ 11 h. The experiments ran for approximately 850 h.

2.3.2 Column experiment

The column experiment consisted of five individual columns (2 cm in diameter and 3 cm in length) connected in sequence with tygon tubes (0.4 cm in diameter and 6 cm in length (Fig. S1), resulting in a total length of 38 cm. Each individual column was filled with a ≈ 1 cm thick layer of glass beads (bottom) and a ≈ 2 cm thick layer of 1-4 mm fragments of the selected sample (top). The function of the glass-bead layer was to homogenize the flow through the fragment layer. Each layer was separated by an inert mesh of 0.45 μm. The first column (c1) was filled with 5.19 g of soil sample #40, the second one (c2) with 6.48 g of waste solid #R6, the third one (c3) with 5.24 g of soil sample #50, the fourth one (c4) with 6.31 g of soil sample #75 and the fifth column (the top one; c5) with 6.10 g of soil sample #200. 0.45 μm filters were placed at the bottom and top of each column to prevent any particle loss (Fig. S1). Considering the volume of the soil layers (6.28 cm^3), the mass and a mineral density of 2.65 g cm^{-3}, the average initial porosity was 65 ± 4 %. To emulate fluid circulation through the soil profile, injection of the input solution (Millipore MQ water) at constant flow rate (0.05 mL min^{-1}) was from the first column upwards. The residence time in each column was about 2 h and the experiment lasted 888 h. Sampling ports were located between c1 and c2 (port-1 from 5 cm from the inlet), between c2 and c3 (port-2 from 14 cm from the inlet), between c3 and c4 (port-3 from 23 cm from the inlet) and between c4 and c5 (port-4 from 32 cm from the inlet). Together with the outlet of the fifth column, the sampling ports enabled us to collect the reacting solution at different column lengths and time intervals. The solutions were collected approximately every 24 h in all sampling port (Fig. S1).

2.3.3. Aqueous Sampling

The pH of the input and output solutions was measured with a combined glass electrode (Crison ^{TM}) at room temperature, yielding pH values with an accuracy of 0.02 pH units. pH calibration was done with standard pH 2, pH 4 and pH 7 buffer solutions.

In all experiments, total concentrations of cations, including total Cr, were analyzed by inductive coupled plasma-atomic emission spectrometry (ICP-AES; Thermo Jarrel-Ash with CID detector and a Perkin Elmer Optima 3200 RL) on samples acidified to pH < 2 with trace-metal grade HNO_3. The accuracy of the measurement was estimated to be 3%. The concentration of dissolved Cr(VI) was measured within 24 h of sample collection using a UV–Vis spectrophotometer (SP-830 plus Metertech) according to the diphenylcarbazide SM 3500-Cr B method (Parks et al., 2004) . The detection limit was 0.01 mg L^{-1}.

The δ^{53}Cr analyses of the output solutions of the column experiment were performed following a slightly modified method by Frei et al. (2009). Solutions were measured using an IsotopX ‘‘Phoenix” multicollector thermal ionization mass spectrometer (TIMS) at temperatures between 1050 ºC and 1200 ºC, aiming at beam intensity at atomic mass unit (AMU) 52.9407 of 30–60 mV. Each load was analyzed 2-4 times. The results are expressed as δ^{53}Cr in per mil (‰) relative to the NIST SRM 979 Cr isotope standard, where:

$$\delta^{53}Cr = \left[\frac{\left(^{53}Cr/^{52}Cr\right)_{sample} - \left(^{53}Cr/^{52}Cr\right)_{SRM979}}{\left(^{53}Cr/^{52}Cr\right)_{SRM979}}\right] \times 1000 \qquad (1)$$

The standard deviation reproducibility of the samples was ± 0.08‰ for δ^{53}Cr.

2.3.4. Isotope data calculations

Under closed system conditions, the isotope fractionation factor (ε) associated with the Cr(VI) reduction can be calculated using the Rayleigh distillation equation

$$\ln\left(\frac{R_{residual}}{R_{initial}}\right) = \varepsilon \times \ln\left(\frac{C_{residual}}{C_{initial}}\right) \qquad (2)$$

where ε is obtained from the slope of the linear correlation between the natural logarithm of the substrate remaining fraction ($\ln(C_{residual}/C_{initial})$, C refers to the analyte concentration and $R = (\delta + 1)$.

2.4. 1D reactive transport modeling

The temporal variation in the aqueous chemistry of the output solution in the R6-sample flow-through experiment and both the temporal and spatial variation of the output solution in the column experiment was reproduced by means of one dimensional (1D) reactive transport modeling using the CrunchFlow code (Steefel et al., 2015). The initial mineral composition of the samples was calculated from the initial mineral composition obtained from the XRD-Rietveld analysis (Tables 2 and 4).

For the flow-through experiment, the 1D numerical domain composed of three nodes with a grid spacing of $2.8 \cdot 10^{-2}$ m was used in the simulations taking into account the experimental residence time. Given the initial mineral mass and cell volume, porosity (ϕ) was close to unity in the experiments ($0.99 < \phi < 1$). For the column experiment, the 1D numerical domain consisted of 300 nodes with a grid spacing of $0.5 \cdot 10^{-3}$ m taking into account that the length of the tubes between columns was calculated dividing the volume of the tube by the column section in order to equal the residence time in both the tube and column. The glass-beads layers were considered to be tube (Fig. S1). Porosity in the columns was 0.65. Solute transport occurred mainly by advection.

In CrunchFlow, solid-phase dissolution and precipitation reactions are always implemented through kinetic reaction rate laws. The rate laws used in the calculations are expressed as

$$R_m = A_m \sum_{terms} k_m a_{H^+}^n \left[1 - \left(\frac{IAP}{Keq}\right)^{m_2}\right]^{m_1} \quad (3)$$

where R_m is the reaction rate (mol m^{-3} s^{-1}), $^{-1}A_m$ is the bulk surface area (m^2 m^{-3}), $k_{m.T}$ is the reaction rate constant at the temperature of interest (mol m^{-2} s^{-1}), a_{H^+} is the activity of H^+ and $a_{H^+}^n$is the term describing the dependence of the rate on pH. The last term in the rate law describes its dependence on the saturation state. *IAP* is the ionic activity product for the solid-phase dissolution reaction and K_{eq} is the equilibrium constant for that reaction (*IAP* at equilibrium). The summation term indicates that several simultaneous parallel rate laws may be considered for any given solid phase. A_m changes with dissolution and precipitation.

The fit of the model to the experimental data was performed by adjusting the mineral surface area term (A_m) within the reaction rate laws (Eq. 1). In the two sets of

simulations, the CO_2 and O_2 concentrations of Milli Q water were in equilibrium with atmospheric CO_2 and O_2 (Table S2), the flow rates were the experimental ones (0.05 mL min^{-1}) and the effective diffusion coefficient (D_{eff}) was calculated making use of the tortuosity (τ), porosity (ϕ) and the molecular diffusion coefficient in pure water ($D_0 = 10^{-9}$ m^2 s^{-1}): $D_{eff} = \phi \cdot \tau \cdot D_0$. The longitudinal dispersivity was 10^{-1} m in the flow-through experiment to ensure that the system was well mixed (no internal concentration gradients within the reactor) and $3 \cdot 10^{-3}$ m in the column experiment. The aqueous species considered in the simulations are listed in Table S3. The stoichiometric coefficients that were taken from EQ3/6 database (Wolery et al., 1990) were included in the CrunchFlow code. Activity coefficients were calculated using the extended Debye Hückel formulation (b-dot model) with parameters obtained from the EQ3/6 database included in CrunchFlow. The solid phases and the log K_{eq} in the calculations are given in Table S4. The initial porewater composition of these samples was assumed to be in equilibrium with the solid phases of the samples at room T and atmospheric pCO_2 (Table S2). The rate parameters used for the minerals are shown in Table 5 where the rate-pH dependence is specified. Cr(VI) adsorption at hydrous ferric oxide (e.g. ferrihydrite) was taken into account by using the surface complexation model developed by Zachara et al. (1987) in which CrO_4^{2-} and H^+ react with the surface site >FeOH to produce two surface sites ($(>FeOH_2^+\text{-}CrO_4^{2-})^-$ and $(>FeOH_2^+\text{-}HCrO_4^{2-})^0$). The concentration of >FeOH was $3.3 \cdot 10^{-6}$ mol m^{-2}, the log$K$ values for the two reactions were 10.1 and 19.3, respectively, and the specific surface area of ferrihydrite was 200 m^2 g^{-1}.

3. RESULTS

3.1. Chemical characterization

The main chemical characteristics of the soil samples (#20 - #200) and the solid waste sample (#R6) are shown in Table 1. According to their chemical composition along the soil profile, the soil samples were divided into two main groups: samples with high S and total Cr contents (group 1) and samples with low S and total Cr contents (group 2). In group 1 (#20,#40, #50, #60, #75, #85 and #100 samples), the Cr contents ranged between 76 and 3997 mg kg^{-1} (average = 1366 ± 1798 mg kg^{-1}). In group 2 (#100,#110, #120, #130, #140, #160, #170, #180 and #200 samples), the con-

tent varied between 33 and 50 mg kg^{-1} (average = 42 ± 7 mg kg^{-1}). These concentrations are close to the levels of the natural chemical background (≈ 30 mg kg^{-1}; Blanco et al. 2012). The content of S displayed a similar pattern. In group 1, S ranged between 7,000 and 21,000 mg kg^{-1} (average = 12,857 ± 4,408 mg kg^{-1}, whereas in group 2 S varied from 1000 to and 14,000 mg/kg (average = 3,625 ± 3,438 mg kg^{-1}). The Ca concentrations in the high Cr and S samples (average = 17,343 ± 6,478 mg kg^{-1}) were lower than in the low Cr and S samples (average = 30,000 ± 8,250 mg kg^{-1}). With the exception of the top soil sample (#20), the concentrations of Al, Na and K were similar in all the soil samples.

In the solid waste sample (#R6), the main elements were Ca, S, Al, Fe and Cr (Table 1). Most of the elements occurred in contents that were lower than those measured in the soil samples. However, the Ca content (86,100 mg kg^{-1}) in the #R6 sample was much higher than that of the soil samples. The content of Cr and S shows contents similar to those measured in the #50 and #60 soil samples (Table 1).

3.2. Mineralogical characterization

3.2.1 Soil samples

Quartz, albite, anorthite, K-feldspar and illite (main clay fraction) were identified in all the soil samples. Gypsum occurred up to 120 cm (sample #20 - sample #120), and calcite was observed in the deepest soil sample (sample #200). Crystalline phases with Cr content were not identified by XRD. However, Cr was detected in the SEM/EDS analysis of samples included in the first meter of the soil profile (e.g. sample #60 in Fig. 1). Grains with planar habit, rich in Cr and associated with Al, Si, S and Fe were observed (Fig. 1a). Some aggregates with granular habit observed onto the planar grains were composed of Cr and Al, Si, S, K, Ca, Ti and Fe (Fig. 1b). Moreover, grains of quartz partially coated with aggregates displaying planar and granular habits (Fig. 1c) were observed. The EDS spectra of these aggregates show the presence of Cr, Al, Si, S, K and Fe.

3.2.2 Solid waste sample

The crystalline phases identified by XRD in the #R6 sample were quartz, gypsum, calcite, illite and ettringite (Fig. S3). SEM images showed the presence of

ettringite crystals with the typical prismatic habit (Fig. 2a), which are similar to those of ettringite described by Palmer (2000) and Song et al. (2019). EDS spectrum of the crystals showed the content of Cr, S and Al. Moreover, other aggregates with acicular habit were identified with contents of Cr together with Ca, S, Si and Al (Fig. 2b). The Ca-Al-Cr based phase could be forming Cr(VI)-hydrocalumite ($Ca_4Al_2(OH)_{12}CrO_4 \cdot 6H_2O$) as discussed in section 4.1. Si was associated with quartz, amorphous SiO_2 and illite.

3.3. Distribution of Cr in the soil solid phases

Table 3 shows the proportions of Cr associated with the dissolved mineral fractions based on sequential extraction. The majority of Cr (58% of the total Cr) was extracted from crystalline Fe(III) oxides fraction (step 4, Table S1). The Cr content found in the low crystalline Fe(III)-oxyhydroxides fraction (step 3) represented between 10% and 36% of the total Cr concentration. The residual fraction (step 6) also represented an important Cr contribution. The Cr released into the soluble fraction (step 1) and into the adsorbed, interchangeable ions fraction or carbonates (step 2) was generally lower than that released in the other steps. In step 1, the proportion of Cr varied between 0.2% and 0.5%, and in step 2 ranged between 8% and 16% (Table 3). The proportion of Cr from the organic fraction was ≈ 1%.

Figure 3 shows the distribution in depth of Cr extracted in each step of the sequential extraction. Overall, the highest Cr released from the different mineral fractions occurs in the first meter of the soil profile. The Cr extracted from the crystalline Fe(III) oxides fraction increases up to the first 50 cm and then decreases with depth. The Cr released from the poorly crystalline Fe(III)-oxyhydroxides fraction displays a similar behaviour. However, in contrast to steps 3 and 4, the total Cr released from the residual fraction is fairly constant with depth from 100 to 200 cm. The Cr released from the organic fraction is mainly detected between 50 and 65 cm depth.

3.4 Flow-through experiments

3.4.1. Soil samples

The output pH during the experiments with the #40, #50 and #75 samples extracted from the first meter of soil ranged between 3.9 and 5.5. In the #200 sample experiment (the deepest sample in the profile), the output pH is higher (between 6.2 and 8) (Fig. 4a). Figure 4b-h displays the temporal trends in outflow Si, Ca, S, Al, K Na and Cr(VI) aqueous concentrations. Overall, the concentrations increase rapidly in the first 20-50 h before decreasing gradually to a steady state at approximately 150 h. There is a marked difference in the release of Si, Ca and Cr between the #200 sample experiment and the experiments with the #40, #50 and #75 samples (Fig. 4b,c,h).

The release of Si in the #200 sample experiment is always much higher. Moreover, it shows a gradual decrease until the end of the experiment, whereas in the other experiments the gradual decrease occurs in the first 100 hours to achieve steady state. A very high Ca release occurs in the experiments with the samples from the first meter of the profile (#40 (3,241 μM), #50 (2,182 μM) and #75 (1,266 μM)) in the first 50 h before a gradual decrease and achievement of steady state at 200 h. However, after 200 h, the Ca concentration in the #200 sample experiment is higher before decreasing until the end of the experiment (Fig. 4c).

The release of S shows a similar trend to that of Ca in the first 50 h for the #40, #50 and #75 soil samples experiments (e.g. 3500 μM; Fig. 4d). Thereafter, it diminishes gradually towards the end of the experiment. In the #200 soil sample experiment, however, the S released is very low during the experiment (between 1.5 μM and 110 μM to). The Al concentration reaches low values (between 100 μM and 160 μM) in the first 50 h in the #40, #50 and #75 soil samples experiments (Fig. 4e). Thereafter, it is even lower (near detection limit) probably due to the low Al solubility at the pH of the experiments. During the #200 soil sample experiment, it is near the detection limit.

K and Na concentrations show similar trends in all the experiments (Fig. 4f,g). The highest release occurs in the first 50 h (60-80 μM in the #200 sample experiment) before a slow decrease towards the end of the experiments. In the experiments with the samples from the first meter of the profile, a rapid Cr(VI) release occurs within the first 20- 50 h (Fig. 4h). Sample #50 shows the highest Cr(VI) concentrations (0.5-6 μM), Thereafter, the concentration falls gradually. Cr(VI) release is negligible in the experiment with the #200 sample (≈ 0.03 μM).

3.4.2. Waste sample

The output pH in the R6 sample experiment (6.7-8.8) is significantly higher than the pH in the experiments with #40, #50 and #75 soil samples (Fig.5a). The average pH is approximately 8 during the experiment.

The release of Ca, S and Si as a function of time shows an initially rapid increase followed by a sharp decrease in Ca and S and a gradual decrease in Si (Fig. 5b-d). The Ca release in the first 50 h is similar to that in the experiments with the #40, #50 and #75 soil samples. Thereafter, Ca gradually decreases until 200 h to achieve steady state with concentrations much higher than those of all the soil sample experiments (between 180 and 200 µM) (Figs. 5b and 4c). The S released in the first 160 h (between 15 µM and 627 µM) is lower than that in the experiments with the #40, #50 and #75 soil samples. Thereafter, it gradually decreases down to 10 µM to 2.5 µM (Fig. 5c). Nevertheless, the S release is higher than that in the #200 soil sample experiment (Figs. 5c and 4d). The Si release is similar to that in the #200 soil sample experiment (Figs. 5d and 4b). The release of K and Mg shows an initially rapid increase followed by a sharp decrease (Fig. 5e). The Al concentration is close to detection limit in the first 200 h (not plotted).

The initial release of Cr(VI) in the solid waste sample experiment is approximately 2-3 orders of magnitude higher than the release in all soil samples experiments (Figs. 5f and 4h), i.e. 436 µM compared with ≈ 0.4-5.8 µM in the soil samples #50 and #75 experiments. Thereafter, the Cr(VI) concentration decreases from ≈ 10 µM to 0.4 µM between 100 h and 860 h (Fig. 5g).

3.5. Column experiment

The temporal variation in the outflow aqueous chemistry is shown in Fig. 6. In the first 100 h, the output pH is slightly alkaline (pH ≈ 8) (Fig. 6a). Subsequently, it falls to circumneutral values (6.7-7.5). This pH range is similar to that in the #R6 solid-waste sample experiment (Figs. 5a and 6a).

The release of Si, Ca, S, Na, K, Mg and Cr(VI) is rapid in the first 72–151 h (Fig. 6b-f). Thereafter, the release of Si, Ca and S gradually falls slowly towards the end of the experiment. By contrast, the release of Na, K and Mg slowly decreases until reaching steady state after approximately 200 h. Al concentrations close to detection limit are detected only in the first 300 h (not plotted). The output Ca and S con-

centrations are similar in the first 200 h (between 12,000 µM and 14,000 µM, respectively). Thereafter, the Ca concentration is higher (Fig. 6c,d), reaching steady state after 600 h ([Ca] = 450-500 µM). By contrast, the S concentration decreases from 600 µM to 200 µM until the end of the experiment (Fig. 6d). The highest Na concentration occurs at 72 h (1,422 µM) (Fig. 6e). The K and Mg concentrations are similar throughout the experiment (Fig. 6e). The highest output Cr(VI) concentration is 322 µM at pH 7.9 (100 h). Thereafter, the Cr(VI) concentration falls from ≈ 148 µM to 9 µM (Fig. 6f).

The temporal variation in the Cr(VI) concentrations along the column is shown in Fig.7a and Fig. S1. At port-1 Cr(VI) concentration is negligible (1.3 µM). The highest Cr(VI) concentration is measured at port-2 (2,518 µM) after 8 h . After 200 h the concentration at ports -3 and -4 is similar to that at port-2. At ports -1, -3 and -4 pH is more acidic (≈ 4) than at port-2 where pH = 7.1 ± 0.9 (Fig. 7b).

Isotopic measurements of Cr(VI) of the output solutions (outlet of c5 column) show a similar isotopic composition. The δ^{53}Cr values range from +2.445‰ to +2.740‰ with an average of +2.63‰ ± 0.1 (Fig. 8a; Table S5). The Cr(VI) concentration measured at port-2 after 8 h was taken as representative for the initial Cr(VI) concentration and isotopic composition because this sample has the highest Cr(VI) content and the sampling port releases Cr(VI) from dissolution of solid waste (c2 column). In c2 column, the δ^{53}Cr value is +2.543 (Fig. 8a; Table S5).

4. DISCUSSION

4.1. Cr(VI) in the soil and solid waste

Multi-acid digestion results show that Cr is mainly concentrated in the first meter of the soil profile, where the soil is in contact with the solid waste. In the solid waste sample, the presence of Cr together with Ca, Al and Fe is similar to the values found by Foldi et al. (2013) and Matern et al. (2016) in COPR samples in Kanpur and in the state of Uttar Pradesh (India). These authors, however, found very low contents of S, unlike the high S contents measured in our work. Foldi et al. (2013) classified the samples with high Cr contents and low S contents as soil-like materials moderately contaminated by COPR. By contrast, in the soil samples of our profile, the contents

of Cr, Ca, Mg, Fe and Al are much lower than the values measured in rCOPR samples treated with ferrous sulfate (Song et al., 2019).

SEP results for the soil samples of this upper zone indicate a probable Cr association with the Fe(III)-oxide and Fe(III)-oxyhydroxide phases (e.g., goethite, jarosite, ferrihydrite, hematite, magnetite, schwertmannite and MnO_2) (Fig. 3, Table S1). Although none of these Cr-phases were identified by XRD, EDS spectra of the soil samples reveal the presence of various compounds rich in Cr-S-K-Fe (Fig. 1b) that could be linked to Cr(VI)-rich jarosite (Fig. 1b). Baron et al. (1996) observed that two types of Fe(III) chromate phases ($KFe_3(CrO_4)_2(OH)_6$ and $KFe(CrO_4)_2 \cdot 2H_2O$) precipitated in acidic soils contaminated with Cr(VI). The highest concentration of Cr(VI) in the acidic soil was found in $KFe_3(CrO_4)_2(OH)_6$ whose structure is analogous to that of jarosite ($KFe_3(SO_4)_2(OH)_6$), which commonly forms in acid sulfate soils. Studying the effect of CrO_4^{2-} on jarosite precipitation at room temperature, Yeongkyoo (2018) showed that the precipitation rate of a highly crystalline CrO_4^{2-}-rich jarosite was rapid and that the CrO_4^{2-} behavior was more influenced by jarosite co-precipitation than by the behavior of other oxyanions (e.g. AsO_4^-). Jarosite co-precipitation thus plays an important role in controlling the CrO_4^{2-} fate in soils affected by acid mine drainage. The low output pH of the flow-through experiments with soil samples from the upper zone (4.8 ± 0.7; Fig. 4a) and the very low release of Cr(VI) (Fig. 4h) suggest that a small amount of Cr-rich jarosite (< 3 wt%) controls the aqueous Cr(VI) concentrations.

In the waste-solid sample, the SEM-EDS analysis confirmed the presence of Cr in ettringite (Fig. 2a), which was identified by XRD (Fig. S3). Cr-rich ettringite commonly forms as CrO_4^{2-} may substitute SO_4^{2-} in this phase, yielding $Ca_6Al_2(OH)_{12}(CrO_4)_3 \cdot 26\ H_2O$ (Palmer, 2000). Hillier et al. (2003) showed the presence of Cr-rich ettringite in COPR materials with an up to 50% CrO_4^{2-} substitution in ettringite crystals. Moreover, in rCOPR treated with ferrous-sulfate, the residual unreacted Cr(VI) exists within the nano-sized ion channels of ettringite (Liu et al., 2020).

In addition to Cr associated with ettringite, the SEM-EDS analysis of our study confirmed the presence of a Ca-Al-Cr compound (Fig. 2b) that could be associated with calcium aluminate phases containing Cr(VI), i.e., hydrocalumite and hydrogarnet. Cr(VI)-bearing hydrogarnet and hydrocalumite were identified in COPR materials (Geelhoed et al., 2002). Hydrogarnet (a calcium aluminate) incorporates

Cr(VI) in the tetrahedral structure by substitution ($(Ca_3(Al,Fe)_2(H_4O_4,CrO_4)_3$ (Hillier et al. 2003, 2007)) and hydrocalumite (Ca-Al-layered double hydroxide with a high anion exchange capacity) incorporates Cr(VI) in the interlayer ($Ca_4Al_2(OH)_{12}CrO_4 \cdot 6H_2O$ (Wazne et al., 2008)). Although these phases were not identified by XRD, small amounts (< 3 wt%) could be present. Note that future transmission electron microspore and selected area electron diffraction (TEM-SAED) analysis is warranted to identify very small amounts of Cr(VI)-rich phases. However, the output pH of 8 in the flow-through experiments with solid waste sample (Fig. 5a) suggests the lack of a Cr(VI)-rich hydrogarnet, which is usually found in high-pH wastes (Hillier et al., 2007). Alternatively, model calculations under equilibrium conditions by Geelhoed et al. (2002) indicated the presence of Cr(VI)-hydrocalumite and Cr(VI)-ettringite at pH between 8 and 11, in which ettringite precipitates during Cr(VI)-hydrocalumite dissolution.

Therefore, the presence of Cr(VI)-ettringite and Cr(VI)-hydrocalumite phases in the solid waste, in addition to calcite and gypsum, suggests that the solid-waste sample of this study is a COPR material. Brucite, calcite, aragonite, ettringite, hydrogarnet and hydrocalumite may form over protracted periods during which COPR material is exposed to ambient operating conditions and to leaching (Hillier et al., 2003). Other studies have determined that gypsum, amorphous SiO_2, dolomite and Al and Fe hydroxide may be present as secondary precipitates (Matern et al., 2016; Farmer et al., 2008; Geelhoed et al., 2002). Even quartz is found in aged COPR samples mixed with natural soil (Bhattacharya et al., 2019). Therefore, the solid waste corresponds to a COPR material mixed with natural soil that has been exposed to weathering, leaching and precipitation of secondary phases.

4.2. Release of Cr(VI) from solid waste

Earlier identification of the solid phases present in the solid waste has enabled us to elucidate the processes responsible for the release of Cr(VI) into the output solutions of the #R6 solid waste sample flow-through experiment by means of reactive transport simulations. In this experiment, the average output pH was slightly alkaline (pH ≈ 8), which is similar to the pH measured in COPR samples mixed with soil

(Foldi et al., 2013). Note, however, that these authors measured highly alkaline pH values (10-12) in pure COPR samples.

Simulations calculate the contribution of each reacting phase to reproduce the output solution composition by adjusting the mineral reactive surface areas (A_m in Eq. (1); Table 4). The A_m values were reduced for all phases relative to the initial reference values except for pyrite that remained the same. Figure 5 depicts the good match between model and measured data. Dissolution of Na_2CrO_4, Cr(VI)-ettringite and Cr(VI)-hydrocalumite led to a slightly alkaline pH until exhaustion (≈ 200 h; Fig. 5a). Thereafter, the output pH was reproduced by dissolving a Mg-rich calcite (10 wt%) and a very low amount of pyrite (< 1 wt%) (Fig. 5a).

Fast dissolution of 3 wt% of Na_2CrO_4 causes the initially high release of Cr(VI) (≈ 150 h; Fig. 5f). Few studies have described the existence of feasible soluble phases (e.g. Na_2CrO_4) in some COPR materials (Chhiwali, India; Matern et al., 2016). Na_2CrO_4 has been linked to crusts containing CrO_4^{2-} salts on the surface of poorly drained soils due to evaporation of water from the soil containing soluble CrO_4^{2}. These crusts usually appeared during dry periods when surface water evaporation occurs (James, 1994). Likewise, the absence of readily soluble phases in COPR materials has been attributed to very old materials (40-180 years), suggesting that these phases have been totally leached (Matern et al., 2016). Since the solid waste in the study area is relatively young (material buried for 30 years) it is highly probable that some Na_2CrO_4 remains.

The gradual decrease in Cr(VI) after N_2CrO_4 is consumed is achieved by the slower dissolution of Cr(VI)-hydrocalumite and Cr(VI)-ettringite with a faster Cr(VI) release from Cr(VI)-hydrocalumite (Figs. 5f and 8b). It has been shown that the release of Cr(VI) is due to dissolution of Cr(VI)-hydrocalumite and Cr(VI)-ettringite that are present in COPR and rCOPR materials derived from the production of Cr(III)-salts used as tanning agents (Foldi et al., 2013). Usually these materials are highly alkaline (pH ≈ 12-13) and natural weathering takes place over decades (Liu et al., 2020). However, little is known about the release of Cr(VI) from the dissolution of these phases when present in slightly alkaline COPR materials mixed with soil. Geelhold et al. (2002) attributed the release of Cr(VI) from COPR material at pH ≈ 9 to the dissolution of Cr(VI)-hydrocalumite. Our calculations suggest that the dissolution of Na_2CrO_4, Cr(VI)-hydrocalumite and Cr(VI)-ettringite causes the release of Cr(VI)

from the COPR material mixed with soil at pH ≈ 8. It is worth mentioning that dissolution of Cr(VI)-hydrogarnet and magnesiochromite ($MgCr_2O_4$) was not included in the calculations because the reactions led to very basic and very acidic pH, respectively, contradicting the experimental output pH (Fig. 5a).

Dissolution of sulfate phases (gypsum, K_2SO_4 and $MgSO_4$) leads to the initially high release of Ca, S, K and Mg (Fig. 5b,c,e). After ≈ 100 h, gypsum, K_2SO_4 and $MgSO_4$ dissolve completely and K concentration depletes, whereas Mg and Ca concentrations are controlled by the dissolution of Mg-rich calcite and Cr(VI)-hydrocalumite. Dissolution of small amounts of pyrite provides some S after the high S concentration peak linked to the dissolution of the sulfate phases. Gypsum in COPR materials together with dolomite, hydrocalumite, ettringite have been related to COPR weathering (Geelhoed et al., 2002). Gypsum has also been identified in soils contaminated with COPR (Glasgow, Scotland; Farmer et al., 2008) and in COPR previously treated by Cr(VI) reductants (e.g. $FeSO_4{\cdot}7H_2O$, Fe(0), CaSx and NaS_2) and deposited yielding pH 8-9 (Wazne et al., 2007; Dermatas et al., 2006). The latter authors evaluated the long-term stability of this rCOPR in which the reduction of Cr(VI) was incomplete preventing the residues from attaining long-term stability during disposal. The presence of secondary K_2SO_4 and $MgSO_4$ is possible in soils that are not necessarily contaminated with COPR but contain K, Na, Mg and sulfate (Lindstrom et al., 2015; Linnov et al., 2014).

Dissolution of amorphous SiO_2 was the main contributor to Si release (Fig. 5d), whereas dissolution of Cr(VI)-hydrocalumite, illite, and feldspars accounted for the very low Al concentration.

4.3. Cr(VI) release and mobility along the column

The solid phases used to simulate both the release and mobility of Cr(VI) along the column are listed in Table 4. To match the experimental data, the A_m values were reduced for calcite, gypsum, silicates and jarosite, increased for pyrite, $SiO_{2(am)}$, Cr(VI-hydrocalumite and Na_2CrO_4, and remained the same for K_2SO_4, $MgSO_4$ and Cr(VI)-ettringite relative to the to the initial reference A_m values. The variation in the output pH in the first 200 h (Fig. 6a) is reproduced with the dissolution of Na_2CrO_4

and Cr(VI)-hydrocalumite. The circumneutral pH observed after 200 h is matched with the dissolution of calcite, pyrite and $SiO_{2(am)}$ (Fig. 6a).

The highest output Cr(VI) concentrations are matched by dissolving Na_2CrO_4, whereas dissolution of Cr(VI)-hydrocalumite and Cr(VI)-ettringite contributes to the Cr(VI) release after 100 h (Figs. 6f and 8b). On the one hand, Cr(VI)-hydrocalumite releases more Cr(VI) than Cr(VI)-ettringite and, on the other hand, Cr(VI)-rich jarosite is very stable without releasing Cr(VI) into solution. Cr(VI)-jarosite belongs to the soil samples of the upper zone in the profile (c1, c3 and c4 columns), whereas the phases that release Cr(VI) constitute the solid waste in c2 column. Since the temporal variation of Cr(VI) is similar at port-2 and at the outlet of the column (Fig. 6f and Fig.7a), it has been put forward that Cr(VI) is only released from the #R6 solid waste (c2 column).

It should be highlighted that the mobility of Cr(VI) is restricted to its aqueous speciation (CrO_4^{2-}, $HCrO_4^-$ and $Cr_2O_7^{2-}$), which depends on the solution pH, initial concentration and on the availability of the ligand. Figure 9 shows the temporal variation in pH and Cr(VI) speciation along the column. The input solution entering the column is acidified by the dissolution of pyrite present in the soil (c1, #40 sample). In the following 3.3-5.3 cm of the column, the solution passes through the solid waste material (c2, #R6 sample) and the dissolution of the Cr(VI)-rich phases raises the pH to above 7. Then, between 6.5 cm and 11.8 cm, the solution acidifies again by dissolution of pyrite (c3 and c4, #50 and #75 samples, respectively). Finally, at the end of the column, the dissolution of calcite present in the soil (c5, #200 sample) increases the pH (Fig. 9a).

Variation in the pH of the solution observed along the column could influence the chemical speciation and Cr(VI) mobility. Geochemical calculations established that the main aqueous Cr(VI) species when the solution circulates through the acid soil columns (c3 and c4) is $HCrO_4^-$, whereas the main species at the outlet of the column is CrO_4^{2-}(Fig. 9b-d). It is well known that at neutral pH, clay minerals (e.g. kaolinite, illite) tend to have a negatively charged surface area which results in Cr(VI) having a low adsorption capacity because electrostatic repulsion (Street and Buchanan, 1956; Acharya et al., 2017). In alkaline pH, competition of excess OH^- ions with CrO_4^{2-} anions for the adsorption sites reduces the adsorption capacity of clays. Bhattacharyya and Sen Gupta (2006) and Frank et al., (2019) observed a maximum

Cr(VI) adsorption on the surface of kaolinite at pH 7.0, after which adsorption diminished. The experimental and model results of Cr(VI) mobility in our column experiment show that the concentration of Cr(VI) does not diminish from c2 (Cr(VI) source) to c5 taking into account the experimental residence time (ca. 6 h; Fig. 9b-d). This suggests that CrO_4^{2-} is not adsorbed on the surface of illite (clay) present in c5 (#200 sample soil) at the end of the column at pH 7.5 (Fig. 9a). In acidic pH, crystalline and amorphous Fe- and Al-oxides have a potential affinity for adsorbing Cr(VI) (Dzombak and Morel, 1990; Ajouyed et al., 2010). Our simulations show, however, that $HCrO_4^-$ is unable to adsorb on the ferrihydrite (≈ 0.3 wt%) that could be present in the acidic soil filling the c3 and c4 columns. This is due to a high initial concentration of Cr(VI) that saturated the surface sites and reduced the adsorption capacity of the Fe(III)-hydroxides.

The mobility of Cr(VI) can also be affected by the oxidation of Fe(II), sulfur and organic carbon present in the medium, which reduces Cr(VI) to Cr(III) generating $Cr(OH)_3$ insoluble precipitates (Blowes, 2002). However, the model results show that Cr(VI) does not reduce (i.e., Cr(III) concentration is negligible). This is confirmed by the isotopic measurements performed in our study that are used to establish if the decrease in Cr(VI) concentrations is due to a reduction process (Wanner et al., 2012). During the reduction of Cr(VI) to Cr(III), a kinetic isotope effect occurs since the lighter isotope (^{52}Cr) reacts preferentially, leaving the remaining dissolved Cr(VI) enriched in the heavier isotope (^{53}Cr). Hence, the calculated change in the isotope ratios (i.e., isotope fractionation (ε)) can be used to assess the Cr(VI) reduction process. According to Jamieson-Hanes et al. (2012) the ε calculated from the experimental data of a column fits better to a linear regression of $\delta^{53}Cr$ vs ln[Cr(VI)] than to a Rayleigh fractionation curve. Figure 8a shows no correlation between these parameters (r^2 = 0.012) with a trend line that indicates a negligible isotope fractionation. Therefore, the decrease in Cr(VI) concentrations was not accompanied by an increase in $\delta^{53}Cr$ values relative to the initial one, suggesting that the decrease in the output Cr(VI) concentration is due to exhaustion of the Cr(VI)-rich phases that release Cr(VI) and not to reduction of Cr(VI) to Cr(III).

In the light of the foregoing discussion, Cr(VI) adsorption or reduction of Cr(VI) to Cr(III) does not affect the Cr(VI) mobility along the column. Hence, at the

study site, leaching of the solid waste mixed with soil releases Cr(VI) that reaches the aquifer as measured by Ceballos et al. (2020).

6. Conclusions

A combination of laboratory experiments, isotopic analyses and reactive transport modelling is essential for a full understanding of the Cr(VI) fate in the contaminated soils with chemical factory waste. The mechanisms and kinetics of Cr release from COPR are poorly understood due to the presence of multiple Cr-containing phases. The novelty of this study is the quantification of the governing processes that enables us to identify the main Cr(VI) contributors, changes in pH and sulphate variation along the soil profile, which is necessary to develop any possible treatment strategy.

On the one hand, results show that the presence of Cr is mainly associated with S, Fe, K and Al in the first meter of the profile as a component of Cr(VI)-rich jarosite (soil phase) and Cr(VI)-rich ettringite and Cr(VI)-bearing hydrocalumite (COPR phases). It is suggested that Cr could have been incorporated in the structure of these SO_4 minerals (CrO_4 substitutes SO_4) as identified by SEM-EDS analyses.

On the other hand, reactive transport simulations indicate that dissolution of small amounts of Cr(VI)-rich ettringite, Cr(VI)-bearing hydrocalumite and Na_2CrO_4 (less than 3 wt%) can account for the Cr(VI) release. By contrast, Cr(VI)-rich jarosite barely dissolves. The presence of jarosite in the site is important from an environmental point of view since this Cr(VI)-rich phase is poorly soluble. Moreover, the solubility of Cr(VI)-ettringite confirms the unstable nature of this typical host phase in rCOPR.

Dissolution of the sulphate phases present in the waste mixed with soil (gypsum, K_2SO_4 and $MgSO_4$) contributes S to the water, enhancing thus groundwater pollution.

Cr(VI) adsorption on Fe-oxyhydroxides (e.g. ferrihydrite) and Cr(VI) reduction to Cr(III) do not occur, preventing thus any natural attenuation. Therefore, mobility of hexavalent chromium along the soil profile is only constrained by the dissolution of available Cr(VI)-containing phases of the COPR-soil mixture.

Acknowledgements

This research was funded by project PICT 2013-2422 (Ministerio de Ciencia, Tecnología e Innovación, MINCYT, Argentina) and project 2021 SGR 00308 (Catalan Government). IDAEA-CSIC is a Centre of Excellence Severo Ochoa (Spanish Ministry of Science and Innovation, Project CEX2018-000794-S funded by MCIN/AEI/10.13039/501100011033). We would like to thank Jordi Bellés and Natàlia Moreno (IDAEA), David Artiga and Maite Romero (SCT-University of Barcelona) for analytical assistance. The authors would like to thank the thoughtful reviews by two anonymous reviewers.

References

Acharya, R., Martha, S., Parida, K. M. 2017. Remediation of Cr (VI) using clay minerals, biomasses and industrial wastes as adsorbents. Advanced materials for wastewater treatment, 129-170.

Ajouyed, O., Hurel, C., Ammari, M., Allal, L. B., Marmier, N. 2010. Sorption of Cr (VI) onto natural iron and aluminum (oxy) hydroxides: effects of pH, ionic strength and initial concentration. J. Haz. Mater. 174, 616-622.

Baron, D., Palmer, C.D., Stanley, J.T. 1996. Identification of two iron− chromate precipitates in a Cr(VI)-contaminated soil. Environ. Sci. Tech. 30, 964-968.

Bhattacharya, M., Shriwastav, A., Bhole, S., Silori, R., Mansfeldt, T., Kretzschmar, R.,Singh, A. 2019. Processes governing chromium contamination of groundwater and soil from a chromium waste source. ACS Earth Space Chem. 4, 35-49.

Bhattacharyya, K. G., Sen Gupta, S. 2006. Adsorption of chromium (VI) from water by clays. Ind. Eng. Chem. Res. 45, 7232–7240.

Blanco, M., Paoloni, J.D., Morrás, H., Fiorentino, C., Sequeira, M.E., Amiotti, N.N., Espósito, M. 2012. Partition of arsenic in soils sediments and the origin of naturally elevated concentrations in groundwater of the southern pampa region (Argentina). Sci. Total Environ. 66, 2075–2084.

Blowes, D. 2002. Tracking hexavalent Cr in groundwater. Science, 295: 2024-2025.

Boecher, T.A., Tinjum, J.M., Xu, H. 2012. Quantification of mineralogical and amorphous species in chromium ore processing residue. J. Resid. Sci. Technol. 9, 131-141.

Burke, T., Fagliano, J., Goldoft, M., Hazen, R. E., Iglewicz, R., McKee, T. 1991. Chromite Ore Processing Residue in Hudson County, New Jersey. Environ. Health Perspect. 92, 131−137.

Ceballos, E., Dubny, S., Othax, N., Zabala, M. E., Peluso, F. 2021. Assessment of human health risk of chromium and nitrate pollution in groundwater and soil of the Matanza-Riachuelo River Basin, Argentina. Exposure and Health 13, 323-336.

Ceballos, E. Margalef-Marti R., Carrey R., Frei R., Otero N. Soler A., Ayora C. 2020. Characterisation of the natural attenuation of chromium contamination in the presence of nitrate using isotopic methods. A case study from the Matanza-Riachuelo River basin, Argentina. Sci. Total Environ. 699, 134331.

Ceballos, E, Bea, S.A., Sanci, R. 2018. Applying reactive transport modelling in a chromium polluted site in the Matanza-Riachuelo Basin, Buenos Aires, Argentina. Int. J. Environ. Heal. R 9, 16-34.

Chrysochoou, M., Fakra, S.C., Marcus, M.A., Moon, D.H., Dermatas, D. 2009. Microstructural analyses of Cr(VI) speciation in chromite ore processing residue (COPR). Environ. Sci. Technol. 43, 5461-5466.

Chrysochoou, M., Dermatas, D. 2007. Application of the Rietveld method to assess chromium(VI) speciation in chromite ore processing residue. J. Hazard. Mater. 141, 370-377.

Dermatas, D., Chrysochoou, M., Moon, D. H., Grubb, D. G., Wazne, M., Christodoulatos, C. 2006. Ettringite-induced heave in chromite ore processing residue (COPR) upon ferrous sulfate treatment. Environ. Sci. Tech. 40, 5786-5792.

Dold, B. 2003. Speciation of the most soluble phases in a sequential extraction procedure adapted for geochemical studies of copper sulfide mine waste. J. Geochem. Explo. 80, 55-68.

Du, Y., Chrysochoou, M. 2020. Microstructural analyses of Cr(VI) speciation in chromite ore processing residue from the soda ash process. J. Hazard. Mater. 393, 122385.

Farmer, J. G., Hillier, S., Lumsdon, D. G., Graham, M. C., & Bewley, R. J. F. 2008. The assessment and remediation of chromite ore processing residue at former disposal sites, Glasgow, Scotland: Current status (2007). In GeoCongress 2008: Geotechnics of Waste Management and Remediation (pp. 740-747).

Farmer, J.G., Paterson, E., Bewley, R.J.F., Geelhoed, J.S., Hillier, S., Meeussen, J.C.L., Lumsdon, D.G., Thomas, R.P., Graham, M.C. 2006. The implications of integrated assessment and modelling studies for the future remediation of chromite ore processing residue disposal sites. Sci. Total Environ. 360, 90-97.

Farmer, J.G., Graham, M.C., Thomas, R.P., Licona-Manzur, C., Paterson, E., Campbell, C.D., Geelhoed, J.S., Lumsdon, D.G., Meeussen, J.C.L., Roe, M.J., Conner, A., Fallick, A.E., Bewley, R.J.F. 1999. Assessment and modelling of the environmental chemistry and potential for remediative treatment of chromium-contaminated land. Environ. Geochem. Health 21, 331-337.

Frank, A. B., Klaebe, R. M., Frei, R. 2019. Fractionation behavior of chromium isotopes during the sorption of Cr (VI) on kaolin and its implications for using black shales as a paleoredox archive. Geochemistry, Geophysics, Geosystems, 20, 2290–2302.

Frei, R., Gaucher, C., Poulton, S.W., Canfield, D.E. 2009. Fluctuations in Precambrian atmospheric oxygenation recorded by chromium isotopes. Nature 461, 250–253.

Földi, C., Dohrmann, R., Matern, K., Mansfeldt, T. 2013. Characterization of Chromium-containing Wastes and Soils Affected by the Production of Chromium Tanning Agents. J. Soils Sediments 13, 1170−1179.

Geelhoed, J. S., Meeussen, J. C., Hillier, S., Lumsdon, D. G., Thomas, R. P., Farmer, J. G., Paterson, E. 2002. Identification and Geochemical Modeling of Pro-

cesses Controlling Leaching of Cr(VI) and Other Major Elements from Chromite Ore Processing Residue. Geochim. Cosmochim. Acta 66, 3927−3942.

Geelhoed, J. S., Meeussen, J. C., Roe, M. J., Hillier, S., Thomas, R. P., Farmer, J. G., Paterson, E. 2003. Chromium remediation or release? Effect of iron (II) sulfate addition on chromium (VI) leaching from columns of chromite ore processing residue. Environ. Sci. Tech. 37, 3206-3213.

Hillier, S., Roe, M. J., Geelhoed, J. S., Fraser, A. R., Farmer, J. G., Paterson, E. 2003. Role of Quantitative Mineralogical Analysis in the Investigation of Sites Contaminated by Chromite Ore Processing Residue. Sci. Total Environ. 308, 195−210.

Hillier, S., Lumsdon, D.G., Brydson, R., Paterson, E. 2007. Hydrogarnet: a host phase for Cr(VI) in chromite ore processing residue (COPR) and other high pH wastes. Environ. Sci. Technol. 41, 1921-1927.

Jamieson-Hanes, J., Gibson, B., Lindsay, M., Kim, Y., Ptacek, C., Blowes, D. 2012. Chromium isotope fractionation during reduction of Cr(VI) under saturated flow conditions. Environ. Sci. Technol. 46, 6783–6789.

Kotas, J., Stasicka, Z. 2000. Chromium occurrence in the environment and methods of its speciation. Environ. Pollut. 107, 263–283.

Köhler, S. J., Dufaud, F., Oelkers, E. H. 2003. An experimental study of illite dissolution kinetics as a function of pH from 1.4 to 12.4 and temperature from 5 to 50 °C. Geochim. Cosmochim. Acta 67, 3583-3594.

Lindström, N., Heitmann, N., Linnow, K., Steiger, M. 2015. Crystallization behavior of $NaNO_3$–Na_2SO_4 salt mixtures in sandstone and comparison to single salt behavior. Appl. Geochem. 63, 116-132.

Linnow, K., Niermann, M., Bonatz, D., Posern, K., Steiger M. 2014. Experimental studies of the mechanism and kinetics of hydration reactions. Energ. Proc. 48, 394-404.

Liu, W., Song, Y., Li, J., Ling, L., Tian, C., Liu, X., Lin, Z. 2020. Efficient extraction of slowly-released Cr(VI) from nano-sized ion channels in Cr(VI)–ettringite from reduced chromite ore processing residue. Environ. Sci.: Nano 7, 1082-1091.

Matern, K., Kletti, H., Mansfeldt, T. 2016. Chemical and Mineralogical Characterization of Chromite Ore Processing Residue from Two Recent Indian Disposal Sites. Chemosphere, 155, 188−195.

Mo, X., Zhou, J., Lin, L., Zhong, Z., Yang, S., Liu, X., Lin, Z. 2020. Extraction of Cr (VI) from chromite ore processing residue via hydrothermal-assisted phase transformation. Chin. Chem. Letters 31, 1956-1960.

Pagnanelli, F., Moscardini, E., Giuliano, V., Toro, L. 2004. Sequential extraction of heavy metals in river sediments of an abandoned pyrite mining area: pollution detection and affinity series. Environ. Pollu. 132, 189–201.

Palandri, J. L., Kharaka, Y. K. 2004. A compilation of rate parameters of water-mineral interaction kinetics for application to geochemical modeling. Geological Survey Menlo Park CA.

Palmer, C. D. 2000. Precipitates in a Cr (VI)-contaminated concrete. Environ. Sci. Tech. 34, 4185-4192.

Parks, J. L., McNeill, L., Frey, M., Eaton, A. D., Haghani, A., Ramirez, L., Edwards, M. 2004. Determination of total chromium in environmental water samples. Water Res. 38, 2827-2838.

Rai, D., Eary, L.E., Zachara, J.M. 1989. Environmental chemistry of chromium. Sci. Total Environ. 86, 15–23.

Singh, R. K.; Sengupta, B.; Bali, R.; Shukla, B. P.; Gurunadharao, V. V. S.; Srivatstava, R. 2009. Identification and Mapping of Chromium (VI) Plume in Groundwater for Remediation: A Case Study at Kanpur, Uttar Pradesh. J. Geol. Soc. India, 74, 49−57.

Sposito G., Lund L., Chang, A. 1989. Trace Metal Chemistry in Arid Zone Field Soil amended with Sewage Sludge. I. Fractionation of Ni, Cu, Zn, Cd and Pb in solid phases. Soil Sci. Soc. Am. J. 46, 260–264.

Song, Y., Li, J., Peng, M., Deng, Z., Yang, J., Liu, W., Shi, Z., Lin, Z. 2019. Identification of Cr(VI) speciation in ferrous sulfate-reduced chromite ore processing residue (rCOPR) and impacts of environmental factors erosion on Cr(VI) leaching. J. Haz. Mater. 373, 389–396.

Steefel C. I., Appelo C. A. J., Arora B., Jacques D., Kalbacher T., Kolditz O., Lagneau V., Lichtner P. C., Mayer K. U., Meeussen J. C. L., Molins S., Moulton D., Shao H., Simunek J., Spycher N., Yabusaki S. B., Yeh G. T. 2015. Reactive transport codes for subsurface environmental simulation. Comput. Geosci. 19, 445-478.

Street, N., Buchanan, A. S. 1956. The ζ-potential of kaolinite particles. Aust. J. Chem. 9, 450-466.

Thomas, R.P., Hillier, S.J., Roe, M.J., Geelhoed, J.S., Graham, M.C., Paterson, E., Farmer, J.G. (2001) Analytical characterisation of solid- and solution-phase chromium species at COPR-contaminated sites. Environ. Geochem. Health 23, 195-199.

Torres E., Auleda M. 2013. A sequential extraction procedure for sediments affected by acid mine drainage. J. Geochem. Expl. 128, 35–41.

Wanner, C., Zink, S., Eggenberger, U., Mäder, U. 2012. Assessing the Cr (VI) reduction efficiency of a permeable reactive barrier using Cr isotope measurements and 2D reactive transport modeling. J. Cont. Hydr. 131, 54-63.

Wazne, M., Jagupilla, S. C., Moon, D. H., Christodoulatos, C., Koutsospyros, A. 2008. Leaching mechanisms of Cr (VI) from chromite ore processing residue. J. Environ. Qual. 37, 2125-2134.

Wazne, M., Jagupilla, S. C., Moon, D. H., Jagupilla, S. C., Christodoulatos, C., Kim, M. G. 2007. Assessment of calcium polysulfide for the remediation of hexavalent chromium in chromite ore processing residue (COPR). J. Haz. Mater. 143, 620-628.

Xu, J., Fan, C., Teng, H. H. 2012. Calcite dissolution kinetics in view of Gibbs free energy, dislocation density, and pCO_2. Chem. Geol. 322, 11-18.

Yeongkyoo, K. 2018. Effects of different oxyanions in solution on the precipitation of jarosite at room temperature. J. Haz. Mater. 353, 118-126.

Zachara, J. M., Girvin, D. C., Schmidt, R. L., Resch, C. T. 1987. Chromate adsorption on amorphous iron oxyhydroxide in the presence of major groundwater ions. Environ. Sci. Tech. 21, 589-594.

Zhang, M., Yang, C., Zhao, M., Yu, L., Yang, K., Zhu, X., Jiang, X. 2018. Immobilization of Cr (VI) by hydrated Portland cement pastes with and without calcium sulfate. *J. Hazard. Mater. 342*, 242-251.

Figure captions

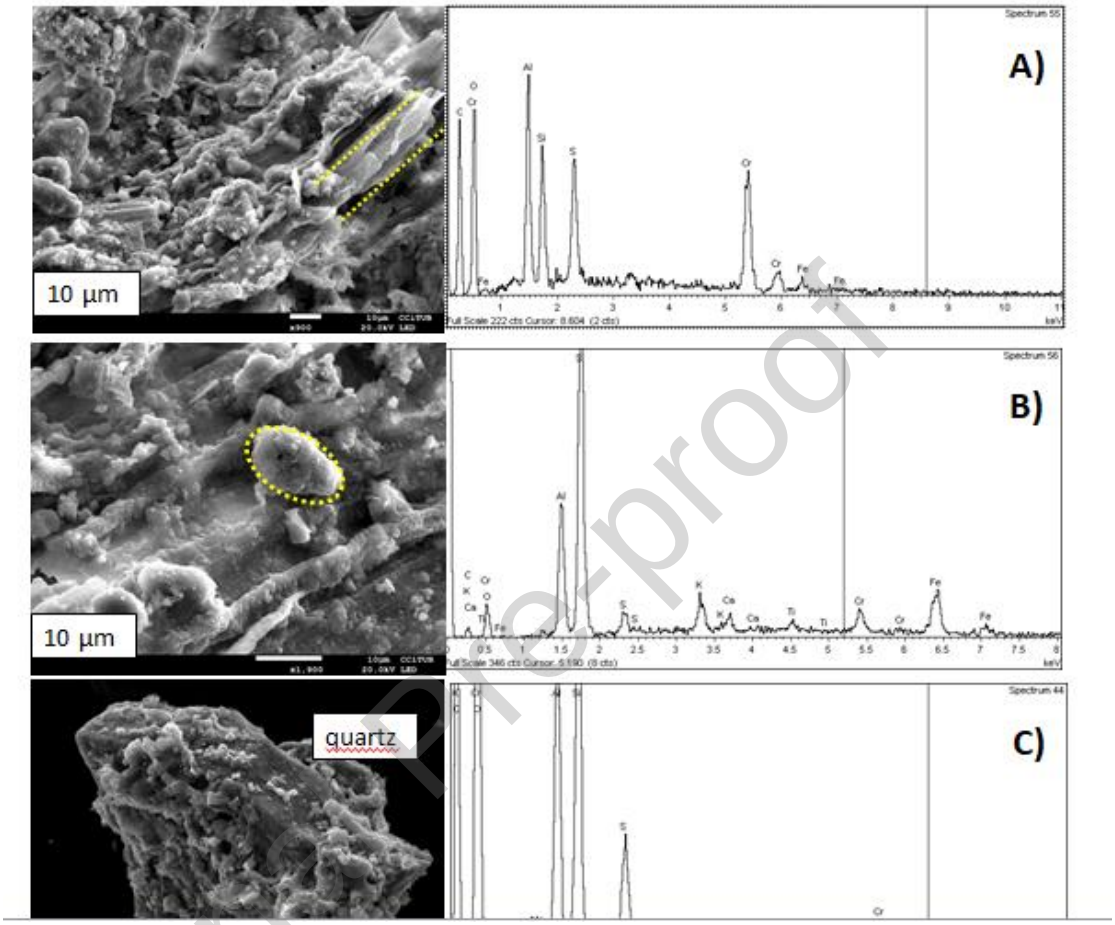

Figure 1 SEM images and EDS spectra of sample #60 extracted from 50-60 cm depth in the soil profile: a) planar crystal (left) with high Cr content (right); b) aggregates with a granular shape (left) with Cr content (right); c) quartz grain partially coated with aggregates of different morphologies (left) and Cr content (right).

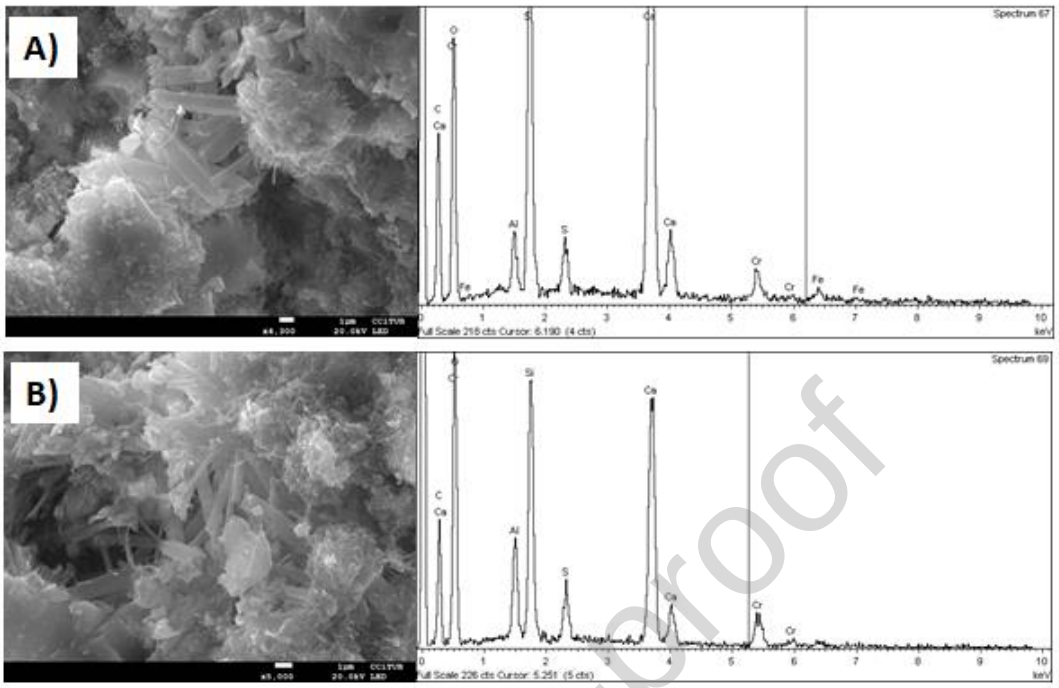

Figure 2 SEM images and EDS spectra of the #R6 sample (see photograph) extracted from solid waste: a) prismatic crystals associated with Cr(VI)-ettringite (left) and related EDS spectrum (right); b) acicular crystals associated with Cr(VI)-hydrocalumite (left) and EDS spectrum of the crystals (right).

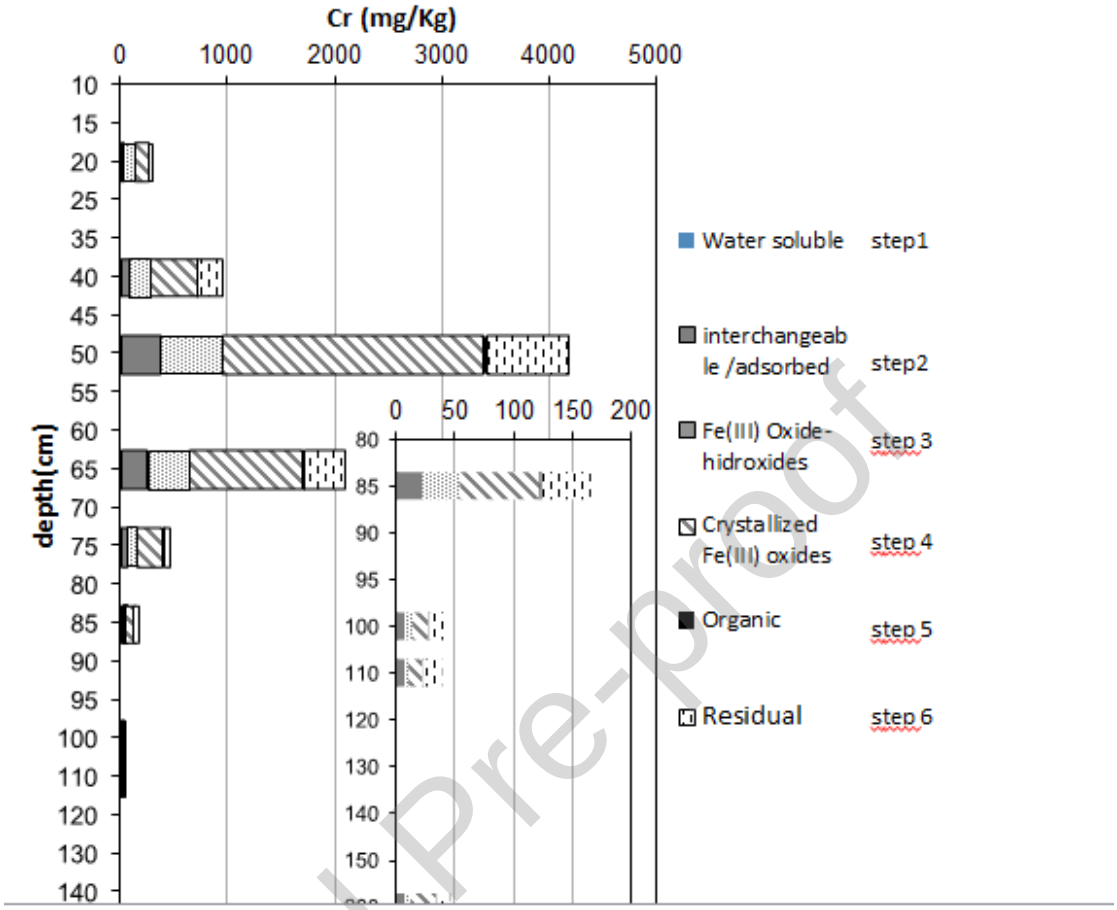

Figure 3 Depth distributions of total Cr in soil. The length of bars account for the total amount and the different fractions are labeled inside.

Figure 4

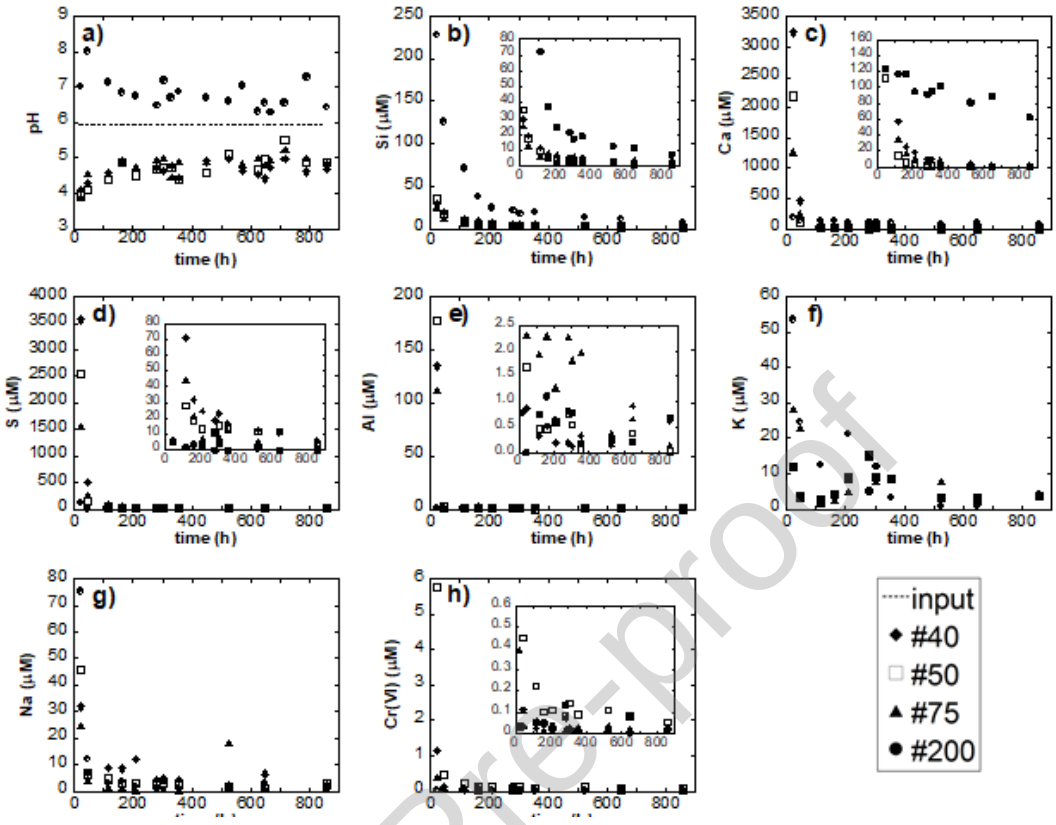

Figure 4 Variation in the outflow pH (a), major elements (b-g) and Cr(VI) (h) concentration as a function of time in the soil samples in the flow-through experiments.

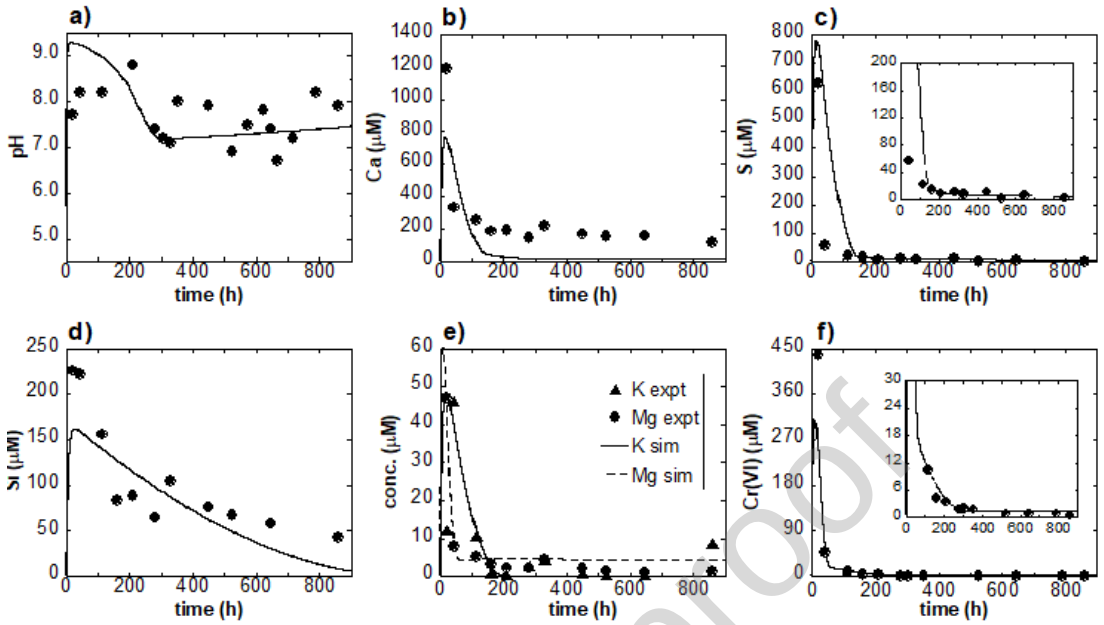

Figure 5 Variation in pH (a) and output concentrations (b-f) as a function of time in the flow-through experiment with solid waste sample; symbols denote experimental data and lines denote model data.

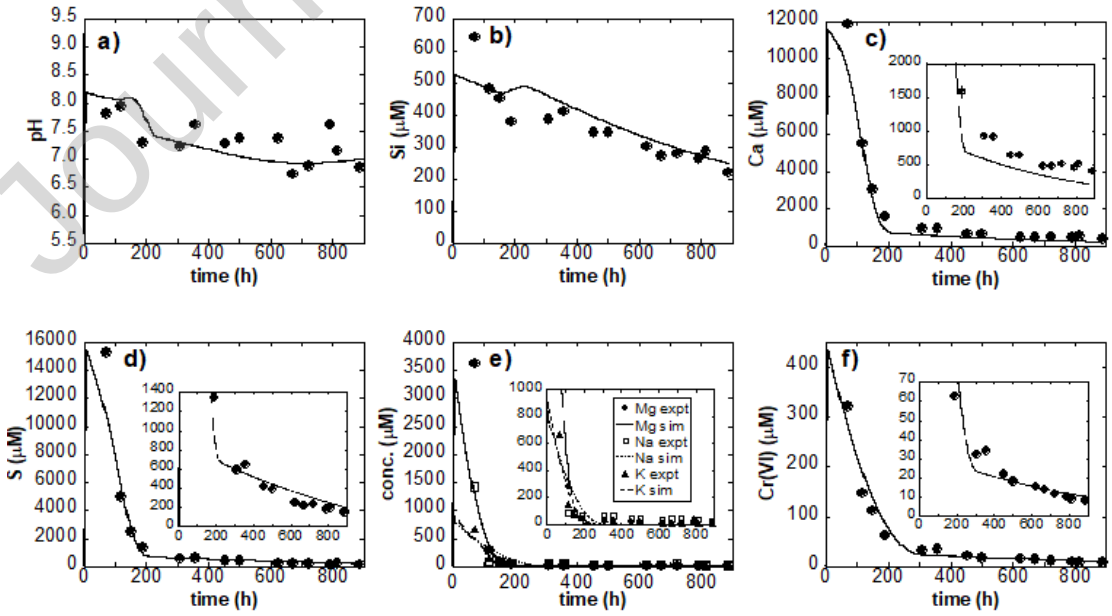

Figure 6 Variation in pH (a) and output concentrations (b-f) as a function of time in the column experiment; symbols denote experimental data and lines denote model data.

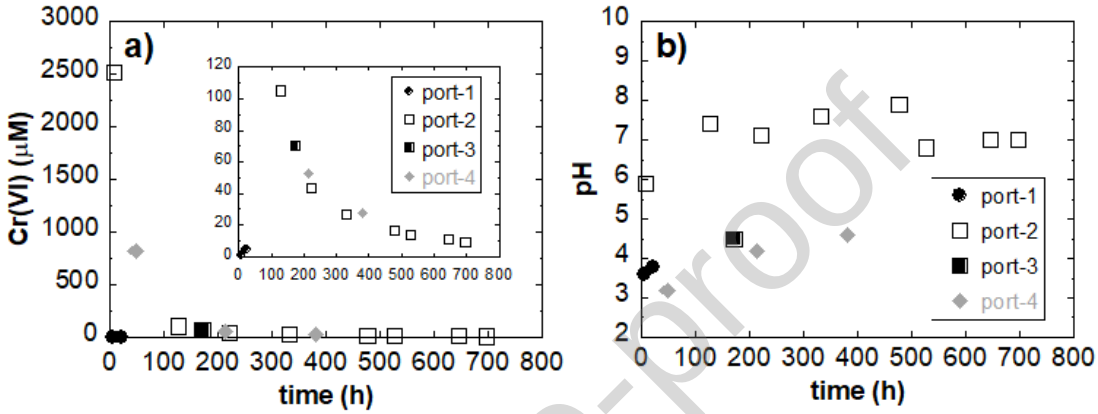

Figure 7 Measured Cr(VI) concentrations (a) and pH (b) at ports 1–4 of the column experiment.

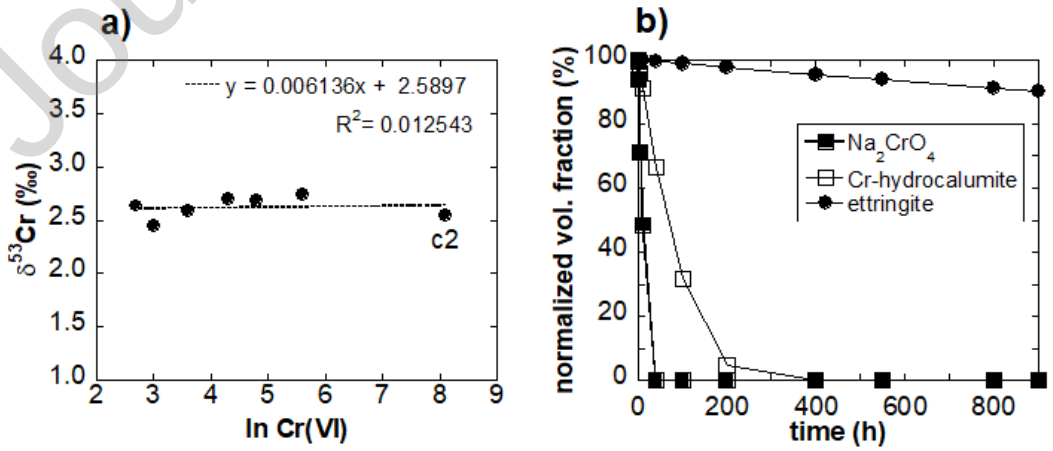

Figure 8 (a) Isotope results for the column experiment plotted as $\delta^{53}Cr$ versus Ln Cr(VI); c2 indicates the initial concentration of Cr(VI) and $\delta^{53}Cr$; (b) Variation of the normalized volume fraction of the Cr-phases as a function of time.

Figure 9

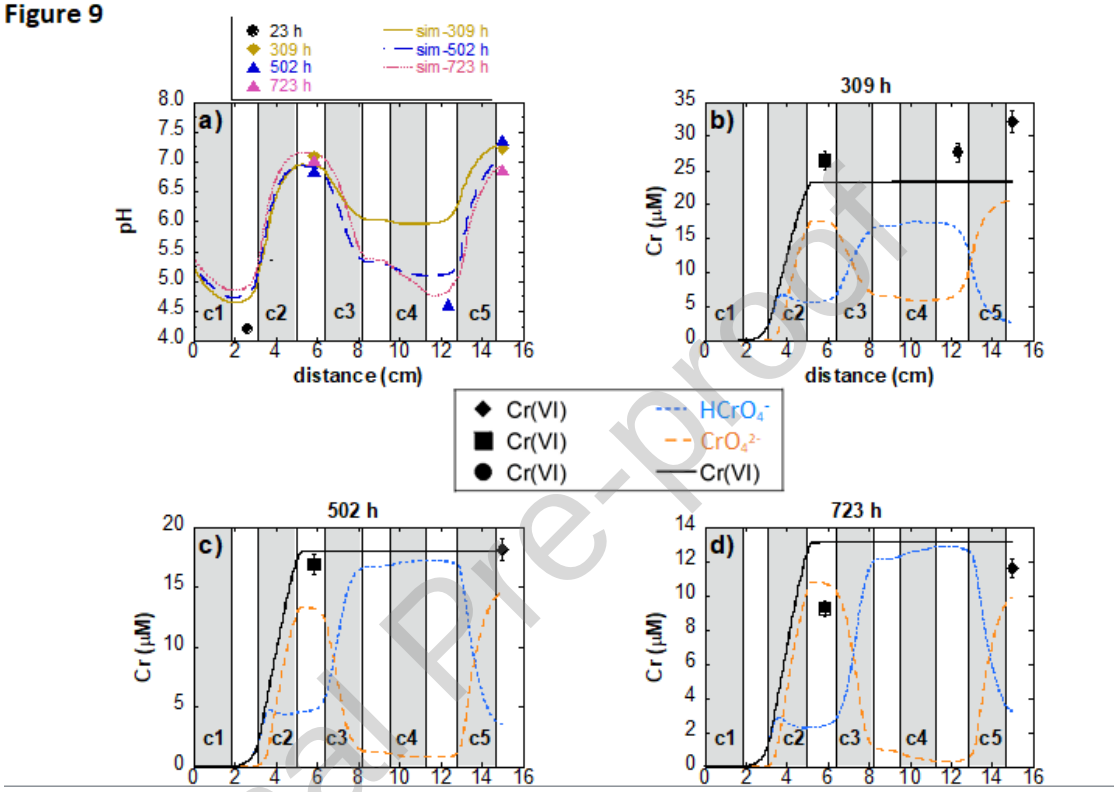

Figure 9 Variation in pH (a) and Cr(VI) concentrations (b-d) along the column at different times (309 h, 502 h and 723 h); symbols = experimental data (square = c2; circle = c4 and diamond = outlet at the different times); line = model data. Cr speciation is also shown. Shaded areas indicate column intervals.

Table heads

Table 1 Concentration of major elements and total Cr of the soil samples (#20 - #200) and solid waste (#R6).

Table 2 Mineralogical composition (wt%) of the samples used in the flow-through and column experiments. Uncertainty is ± 10%.

Table 3 Sequential extraction of soil samples: content of total Cr in the different mineral fractions (wt%).

Table 4 Mineral volumetric fractions and reactive surface areas used in the modeling.

Table 5 Rate constants (log *k*) and kinetic parameters for the minerals employed in the modeling of the #R6 (solid waste) flow-through and column experiments.

Table 1 Concentration of major elements and total Cr of the soil samples (#20 - #200) and solid waste (#R6).

s **ample**	**d** **epth** (cm)	**a**		**a**	**g** (mg/kg)	**n**	**e**	**l**		**r**
# 20	0 -20	,820	,700	,900	00	55	2,800	4,300	,000	03
# 40	2 0-40	1,680	3,500	7,100	,900	25	5,600	1,600	1,000	52
# 50	4 0-50	2,780	3,700	4,200	,600	38	3,000	8,900	1,000	,968
# **R6**	**4** **0-50**	**,130**	**,100**	**6,100**	**,500**	**25**	**,000**	**,900**	**0,000**	**,607**
# 60	5 0-60	4,110	5,100	8,900	,300	94	7,500	8,800	5,000	,997
# 75	6 0-75	5,160	7,000	5,400	,200	32	8,300	2,500	0,000	79
# 85	7 5-85	3,760	7,500	5,200	,700	97	2,900	6,400	,000	85
#	8									

100	5-100	2,870	6,600	8,700	,200	82	2,400	2,900	8,000	6
	# 1									
110	00-110	3,930	7,100	5,900	0,000	,563	2,000	6,300	4,000	9
	# 1									
120	10-120	5,720	7,900	2,400	1,000	96	2,000	2,000	,000	0
	# 1									
130	20-130	9,410	8,600	5,700	,900	56	0,300	2,100	,000	2
	# 1									
140	30-140	9,060	8,700	0,100	,700	84	0,000	1,800	,000	0
	# 1									
160	40-160	8,150	8,100	5,300	,600	12	9,300	2,700	,000	0
	# 1									
170	60-170	4,520	5,600	8,000	,700	50	8,300	4,300	,000	3
	# 1									
180	70-180	5,040	6,100	2,600	,300	95	7,900	5,200	,000	3
	# 1									
200	80-200	5,020	6,500	0,000	,300	70	7,700	4,500	1,000	8

Table 2 Mineralogical composition (wt%) of the samples used in the flow-through and column experiments. Uncertainty is ± 10%.

phase	**sample**				
	#40	#50	#75	#200	#R6
quartz	32	43	28	33	72
illite	15	12	14	10	2
anorthite	13	20	20	17	-
albite	24	18	19	20	
K-feldspar	-	-	15	11	-
calcite	-	-	-	9	11

gypsum	16	4	6	-	8
ettringite	-	-	-	-	7

Table 3 Sequential extraction of soil samples: content of total Cr in the different mineral fractions (wt%).

sample	**soluble**	**adsorbed and interchangeable ions**	**Fe(III) oxide-hydroxides**	**Fe(III) oxides**	**organic**	**residual**
#20	0.4	11.2	35.6	7.5	0.4	4.9
#40	0.4	8.9	20.7	5.2	0.5	4.3
#50	0.3	8.6	14.0	7.9	1.1	8.2
#60	0.3	11.8	18.4	0.8	0.7	7.9
#75	0.4	12.7	19.9	2.5	0.9	3.5
#85	0.3	13.1	19.1	1.1	0.6	5.8
#100	0.3	15.9	14.8	3.8	0.4	4.8
#110	0.5	15.0	10.4	1.0	0.4	2.8
#200	0.3	12.8	11.4	9.5	0.4	5.6

Table 4 Mineral volumetric fractions and reactive surface areas used in the modeling.

olid phase	volumetric fraction (%)						geometric A_m (m^2_{min} m^{-3}_{bulk})						adjusted A_m (m^2_{min} m^{-3}_{bulk})					
	low-through	column					low-through	column					low-through	column				
	R6	1	2	3	4	5	R6	1	2	3	4	5	R6	1	2	3	4	5
alcite						.9						.6E+02						.7E+01
g-rich calci-te	.08		.3				.1E+03		.7E+02				.8E+01		.0E+01			
ypsum	.05	.9	.3	.3	.9		.1E+03	.9E+02	.4E+02	.3E+02	.7E+02		.2E+02	.0E+00	.5E+00	.0E-02	.0E-02	
llite	.01	.4	.7	.8	.3	.7	.4E+03	.4E+02	.7E+01	.6E+02	.1E+02	.1E+02	.0E+00	.0E-03	.0E-06	.0E-06	.0E-05	.0E-05
uartz	.4	.7	4.7	3.2	0.2	1.7	.4E+04	.6E+02	.2E+03	.3E+03	.4E+02	.8E+02	.0E-05	.0E-05	.0E-07	.0E-07	.0E-07	.0E-07
iO_2(am)	.03	.6	.9	.9	.5	.7	.0E+03	.7E+01	.2E+01	.0E+01	.2E+02		.3E+02	.5E+04	.0E+03	.0E+03	.0E+03	.0E+03
yrite	.002	.04	.09	.06	.08		.0E+02	.6E+00	.8E+00	.0E+00	.0E+00		.0E+02	.3E+04	.0E+04	.0E+04	.0E+04	
northite		.1		.3	.6	.2		.1E+03		.2E+03	.1E+03	.3E+02		.0E+00		.0E+01	.0E+01	.0E+00

lbite		.5		.7	.2	.3		.0E+02		.4E+02	.8E+02	.2E+02		.0E+00		.0E+01	.0E+00	.0E-01
-feldspar					.8	.0					.0E+02	.3E+02					.0E+00	.0E+00
$_2SO_4$	.001	.06	.07	.06	.08		.5E+02	.0E+00	.0E+00	.0E+00	.0E+00		.2E-01	.0E+00	.0E+00	.0E+00	.0E+00	
gSO_4	.001	.3	.4	.3	.4		.1E+02	.0E+01	.0E+01	.0E+01	.0E+01		.0E-01	.0E+01	.6E+01	.0E+01	.0E+01	
a_2CrO_4	.01		.4				.5E+02		.0E+01				.0E+01		.7E+02			
r(VI)-jarosite		.2		.2	.1			.5E+01		.5E+01	.1E+01			.0E-02		.0E-02	.0E-02	
r(VI)-et-tringite	.05		.7				.3E+03		.2E+02				.0E+00		.0E+02			
r(VI)-hydrocalumite	.01		.4				.1E+03		.6E+01				.0E+01		.1E+03			
orosity	9.3	9.0	3.0	9.0	2.0	3.0												

Table 5 Rate constants (log *k*) and kinetic parameters for the minerals employed in the modeling of the #R6 (solid waste) flow-through and column experiments.

solid phase	**log *k***	$_{H+}^{n}$	**1**	**2**	**reference**

	(mol m^{-2} s^{-1})				
calcite-a [$CaCO_3$]	-0.3				1
calcite-n [$CaCO_3$]	-5.8				1
Mg-rich calcite-a [$Ca_{1.5}Mg_{0.5}(CO_3)$]	-0.3				2
Mg-rich calcite-n [$Ca_{1.5}Mg_{0.5}(CO_3)$]	-5.8				2
gypsum [$CaSO_4.2H_2O$]	-2.8				2
illite-a [$(K_{0.6}Mg_{0.25})(Si_{3.5},Al_{2.3})O10[(OH)2]$]	-3.7	.6			3
illite-n	-12.6				3
illite-b	-0.6	0.6			3
quartz-a [SiO_2]	-13.4	.30			2
quartz-n	-16.3	0.5			2
SiO_2(am)	-12.2				2
pyrite [FeS_2]	-7.5	.5			2
anorthite-a [$CaAl_2Si_2O_8$]	-3.5	.41	4	.4	2
anorthite-n	-9.1		4	.4	2
albite-a	-9.9	.46	5	.3	2
albite-n	-12.0		5	.3	2
albite-b	-17.0	0.6	5	.3	2
K_2SO_4	-2.8				4
$MgSO_4$	-2.8				4
Na_2CrO_4	-6.0				5
Cr(VI)-jarosite [$KFe_3(CrO_4)_2(OH)_6$]	-8.0				5
Cr(VI)-ettringite [$Ca_6Al_2(OH)_{12}(CrO_4)_3$ 26] H_2O	-8.0				5
Cr(VI)-hydrocalumite [$Ca_4Al_2(OH)_{12}CrO_4 \cdot 6H_2O$]	-8.0				5

-a = acid pH; -n = neutral pH; -b = basic pH

1: Xu et al. (2012) Chem. Geol. 322, 11-18.

2: Palandri and Kharaka (2004) Geological Survey Menlo Park CA.

3: Khöler et al. (2003) Geochim. Cosmochim. Acta 67,

3583-3594.

4: same as gypsum

5: fitted values to match the exp mental data

CRediT authorship contribution statement

Ceballos E. Conceptualization; Investigation; Funding acquisition; Methodology; Writing - original draft.

Cama, J. Investigation; Funding acquisition; Supervision; Writing - review & editing.

Soler, J.M Investigation; Funding acquisition; Supervision; Writing - review & editing.

Frei R. Investigation; Methodology; Writing - review & editing.

Declaration of Competing Interest

☒The authors declare that they have no known competing financial interests or personal relationships that could have appeared to influence the work reported in this paper.

☐The authors declare the following financial interests/personal relationships which may be considered as potential competing interests:

Environmental Implication

Chromium-ore processing residues (COPR) contain large amounts of Cr(VI). Non-stable Cr(VI)-rich phases in these wastes liberate Cr(VI), which pollutes groundwater. In this study, we quantify the mechanisms that control both the Cr(VI) release and Cr(VI) mobility in contaminated soil, resulting in a better understanding of the Cr(VI) fate in the vadose zone. It is shown that small fractions of Cr-rich phases are the source of harmful Cr(VI) and that reduction of Cr(VI), i.e., natural attenuation, does not occur. These results are relevant for an efficient mitigation of Cr(VI) in contaminated soils.

Graphical abstract

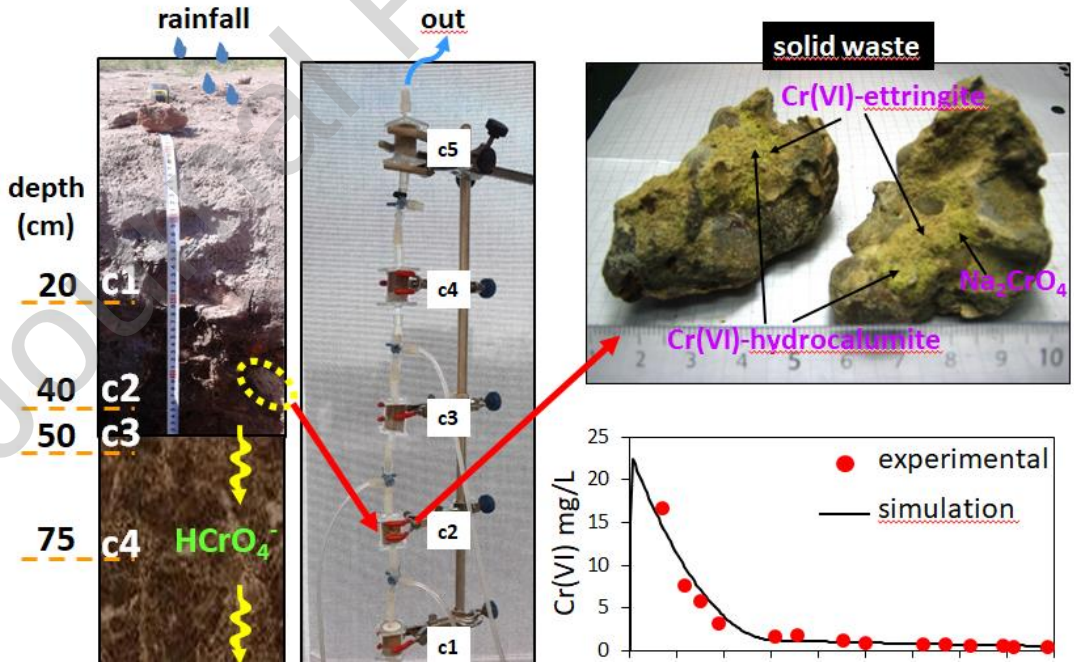

Highlights

Experimental and reactive transport modeling study of solid Cr-waste mixed with soil

Solid waste contains Cr(VI)-rich phases (e.g. ettringite, Cr-hydrocalumite)

Dissolution of small amounts of Cr(VI)-rich phases and Na_2CrO_4 release Cr(VI)

Adsorption and reduction of Cr(VI) do not affect Cr(VI) mobility